PHYSICAL REVIEW D VOLUME 50, NUMBER 1 1 JULY 1994

Exclusive $W^+ + \gamma$ production in proton-antiproton collisions. II. Results

S. Mendoza and J. Smith

Institute for Theoretical Physics, State University of New York at Stony Brook, Stony Brook, New York 11794-3840

(Received 18 February 1994)

We present results for total cross sections, single and double differential distributions, and correlations between pairs of outgoing particles in the reactions $p+\bar{p}\rightarrow W^+ + \gamma$ and $p+\bar{p}\rightarrow W^+ + \gamma +$jet at $\sqrt{S}=1.8$ TeV. Order α_S QCD corrections and leading logarithm photon bremsstrahlung contributions are included in the $\overline{\text{MS}}$ mass factorization scheme for three experimental scenarios: (1) two-body inclusive production of W^+ and γ, (2) exclusive production of W^+, γ, and 1 jet, and (3) exclusive production of W^+ and γ with 0 jets. The latest CTEQ parton distribution functions, which fit the newly released data from DESY HERA, are used in our analysis. The dependence of our results on the mass factorization scale is used to place error bars on our predictions for the single differential distributions and correlations.

PACS number(s): 13.85.Hd, 12.38.Bx, 14.70.Fm

I. INTRODUCTION

In the first part of this study [1] we presented the general formalism for the computation of exclusive cross sections in $p+\bar{p}\rightarrow W^+ + \gamma$ and $p+\bar{p}\rightarrow W^+ + \gamma +$jet. We examined the order α_S and photon bremsstrahlung contributions to these cross sections in the modified minimal subtraction ($\overline{\text{MS}}$) mass factorization scheme. The analytical expressions obtained in that work were then combined with a Monte Carlo integration routine, namely, VEGAS [2], to produce numerical results for three different experimental scenarios: (1) two-body inclusive production of W^+ and γ, (2) exclusive production of W^+, γ, and one jet, and (3) exclusive production of W^+ and γ with zero jets. The resulting programs have been run for $\sqrt{S}=1.8$ TeV in the proton-antiproton center of mass system (Fermilab Tevatron). We include 4 massless flavors u, d, s, and c in our partonic hard scattering processes and set $\cos\theta_C=0.95$ where θ_C is the Cabibbo angle. We use the one-loop strong running coupling constant with $\Lambda_{\text{QCD}}=0.139$ GeV. The W boson is assumed to be an on-shell physical particle with mass $M_W=80.2$ GeV.

We use the latest available CTEQ parton distribution functions [3] in the $\overline{\text{MS}}$ mass factorization scheme (set CTEQ2M). These parton distribution functions are in agreement with the latest CCFR next to leading order (NLO) analysis of the strange quark density and fit the newly released data from the DESY ep collider HERA (for details, see [3]).

The three experimental scenarios considered here are defined as follows (see also the discussion in [1]).

A. Two-body inclusive production of W^+ and γ

In this scenario ("two-body inclusive scenario") the reaction $p+\bar{p}\rightarrow W^+ + \gamma + X$ with $X=0$ or 1 jet is considered. In other words, one detects the outgoing W^+ boson and the photon but does not tag the outgoing jet. We therefore use the following kinematic restrictions on the outgoing particles, in the proton-antiproton center of mass frame:

$$
\begin{aligned}
&|\cos\theta_\gamma|, |\cos\theta_W| < \cos(0.3\ \text{rad})\ ,\\
&P_{t\gamma}, P_{tW} > 10.0\ \text{GeV}\ ,\\
&R_{W,\gamma} > 0.2\ , \qquad\qquad (1.1)\\
&(R_{\text{jet},\gamma} < 0.2) \Longrightarrow (s_{(\text{jet},\gamma)} < 0.2)\ ,\\
&(R_{\text{jet},W} < 0.2) \Longrightarrow (s_{(\text{jet},W)} < 0.2)\ ,
\end{aligned}
$$

where θ_i is the angle between the incoming proton axis and the axis of the outgoing particle i and P_{ti} is the transverse momentum of particle i. $R_{i,j}$ is the cone size between a pair of outgoing particles: $R_{ij}=\sqrt{(\eta^*_{i,j})^2+(\phi_{i,j})^2}$ with η^* the pseudorapidity and ϕ the azimuthal angle; $s_{(\text{jets},W)}=E_{\text{jet}}/E_W$ is the "shadowing ratio" between the untagged jet and the W^+ boson. The third condition in (1.1) removes events where the W^+ boson is too close to the photon. The last two conditions remove events where the jet which is too close to the W^+ boson or photon is at the same time of comparable energy, so that it would "shadow" one of the two tagged particles, making it undetectable. This might be the case for bremsstrahlung contributions with small photon momentum fraction.

Several artificial parameters, namely, x_0, y_0, and v_0 were introduced in [1] in order to control the numerical cancellation of singularities. Results for physical quantities such as total cross sections and differential distributions and correlations do not depend on the choice of these parameters; however, the requirement of stability and small numerical errors in the Monte Carlo runs lead us to the choice $x_0=[1+\rho(s)]/2$, $y_0=1.0$ for the partial cross sections in the $q\bar{q}$ channel and $y_0=v_0=0.05$ for the partial cross sections in the qg and $g\bar{q}$ channels. For the cut parameters defined in Sec. V of [1] we choose the values $\Delta_x=10^{-5}$ and $\Delta_y=\Delta_v=10^{-8}$. As discussed in the referred section these cuts introduce errors in the numeri-

0556-2821/94/50(1)/251(15)/$06.00

cal results; however, we have checked that the above choice minimizes these errors while keeping the Monte Carlo program stable. Our tables of results for total cross sections include entries for the lowest order estimates of these errors and confirm that they are negligible. Thus the expressions for the errors are neglected in all the distributions and correlations.

B. Exclusive production of W^+, γ, and one jet

In this scenario ("one-jet scenario") one detects three outgoing particles: namely, the W^+, γ, and one jet. This scenario is thus defined by the kinematic conditions

$$\begin{aligned}
&|\cos\theta_\gamma|, |\cos\theta_W|, |\cos\theta_{\text{jet}}| < \cos(0.3 \text{ rad}) , \\
&P_{t\gamma}, P_{tW}, P_{t\,\text{jet}} > 10.0 \text{ GeV} , \\
&R_{W,\gamma} > 0.2 , \\
&R_{\text{jet},\gamma} > 0.2 , \\
&R_{\text{jet},W} > 0.2 .
\end{aligned} \tag{1.2}$$

The above conditions will automatically remove bremsstrahlung contributions which tend to produce jets parallel to the outgoing photon. In the Monte Carlo runs we choose the values for the artificial parameters of this scenario in all channels as $x_0 = 1, y_0 = v_0 = 0$. This choice and the above cuts guarantee that no unphysical dependence is introduced in the calculation of physical quantities related to the jet. Moreover, the cuts $\Delta_x, \Delta_y, \Delta_v$ introduced in the first scenario are not necessary here and thus the associated errors are zero in this case.

C. Exclusive production of W^+ and γ with zero jets

In this scenario ("zero-jet scenario") we select events where the W^+ boson and the photon are detected and no outgoing jet is detected. This will include two- and three-body events where the outgoing jet is not detected because it has either a small angle with respect to the beam or a small transverse momentum or it is "shadowed" by the W^+ boson or the photon. The following kinematic conditions define this scenario:

$$\begin{aligned}
&|\cos\theta_\gamma|, |\cos\theta_W| < \cos(0.3 \text{ rad}) , \\
&P_{t\gamma}, P_{tW} > 10.0 \text{ GeV} , \\
&R_{W,\gamma} > 0.2 , \\
&(R_{\text{jet},\gamma} < 0.2) \Longrightarrow (s_{(\text{jet},\gamma)} < 0.2) , \\
&(R_{\text{jet},W} < 0.2) \Longrightarrow (s_{(\text{jet},W)} < 0.2) , \\
&[|\cos\theta_{\text{jet}}| > \cos(0.3 \text{ rad})] \text{ or } (P_{t\,\text{jet}} < 10.0 \text{ GeV}) .
\end{aligned} \tag{1.3}$$

As already discussed in [1], the results for this scenario can be obtained by subtracting the results for the one-jet scenario from the corresponding results for the two-body inclusive scenario.

In Sec. II we present results for total cross sections. Section III is devoted to the discussion of single differential distributions and correlations. In Sec. IV we present and discuss results for double differential cross sections and correlations. In Sec. V we end our study with some concluding remarks.

II. TOTAL CROSS SECTIONS

A. Brief review of relevant formulas

We write the total hadronic cross section as

$$\sigma^H = \int_0^1 d\tau_1 \int_0^1 d\tau_2 \{ f_{qp}(\tau_1) f_{\bar{q}\bar{p}}(\tau_2) \sigma_{q\bar{q}} + f_{qp}(\tau_1) f_{g\bar{p}}(\tau_2) \sigma_{qg} + f_{gp}(\tau_1) f_{\bar{q}\bar{p}}(\tau_2) \sigma_{g\bar{q}} + (p \leftrightarrow \bar{p}, \tau_1 \leftrightarrow \tau_2, p_1 \leftrightarrow p_2, P_1 \leftrightarrow P_2) \} , \tag{2.1}$$

with

$$\begin{aligned}
\sigma_{q\bar{q}} &= \sigma^{\text{Born}}_{q\bar{q}} + \sigma^P_{q\bar{q}(\text{SV})} + \sigma_{\text{Ia}} + \sigma_{\text{Ib}} + \sigma_{\text{I},4} + \sigma^P_{q\bar{q}(\text{finite})} + \sigma_{q\bar{q}(\text{brems})} + \sigma_{q\bar{q}(\text{error})} , \\
\sigma_{qg} &= \sigma^{P,\text{I}}_{qg,\text{finite}} + \sigma^{\text{I,col}}_{qg} + \sigma^{P,\text{II}}_{qg,\text{finite}} + \sigma^{\text{II,col}}_{qg} + \tilde{\sigma}^P_{qg} + \sigma_{qg(\text{brems})} + \sigma_{qg(\text{error})} , \\
\sigma_{g\bar{q}} &= \sigma^{P,\text{I}}_{g\bar{q},\text{finite}} + \sigma^{\text{I,col}}_{g\bar{q}} + \sigma^{P,\text{II}}_{g\bar{q},\text{finite}} + \sigma^{\text{II,col}}_{g\bar{q}} + \tilde{\sigma}^P_{g\bar{q}} + \sigma_{g\bar{q}(\text{brems})} + \sigma_{g\bar{q}(\text{error})} ,
\end{aligned} \tag{2.2}$$

and

$$\begin{aligned}
\sigma_{\text{Ia}} &= \sigma_{\text{Ia},1} + \sigma_{\text{Ia},2} + \sigma_{\text{Ia},3} , \\
\sigma_{\text{Ib}} &= \sigma_{\text{Ib},1} + \sigma_{\text{Ib},2} + \sigma_{\text{Ib},3} , \\
\sigma^P_{q\bar{q}(\text{finite})} &= \sigma_{f,1,1,\text{a}} + \sigma_{f,1,2,\text{a}} + \sigma_{f,1,3,\text{a}} + \sigma_{f,1,1,\text{b}} + \sigma_{f,1,2,\text{b}} + \sigma_{f,1,3,\text{b}} \\
&\quad + \sigma_{f,2,1,\text{a}} + \sigma_{f,2,2,\text{a}} + \sigma_{f,2,3,\text{a}} + \sigma_{f,2,1,\text{b}} + \sigma_{f,2,2,\text{b}} + \sigma_{f,2,3,\text{b}} + \sigma_{f,3} , \\
\sigma^{P,\text{I}}_{qg,\text{finite}} &= \sigma^{\text{I}}_{qg,f,1} + \sigma^{\text{I}}_{qg,f,2} + \sigma^{\text{I}}_{qg,f,3} , \\
\sigma^{P,\text{II}}_{qg,\text{finite}} &= \sigma^{\text{II}}_{qg,f,1} + \sigma^{\text{II}}_{qg,f,2} + \sigma^{\text{II}}_{qg,f,3} , \\
\sigma^{P,\text{I}}_{g\bar{q},\text{finite}} &= \sigma^{\text{I}}_{g\bar{q},f,1} + \sigma^{\text{I}}_{g\bar{q},f,2} + \sigma^{\text{I}}_{g\bar{q},f,3} , \\
\sigma^{P,\text{II}}_{g\bar{q},\text{finite}} &= \sigma^{\text{II}}_{g\bar{q},f,1} + \sigma^{\text{II}}_{g\bar{q},f,2} + \sigma^{\text{II}}_{g\bar{q},f,3} .
\end{aligned} \tag{2.3}$$

Each term in (2.2) and (2.3) has been explained in Sec. V of [1]. Note that the replacements in parentheses in (2.1) apply to all explicit as well as implicit variables in the above expressions. The last replacement in the parentheses in (2.1) will act on physical variables that go into experimental cut functions and histograms (see Sec. IV D of [1]).

For the bremsstrahlung contributions we use here the so called leading logarithm approximation, which has been previously used by other authors [4–6]. In this approximation we write the photon fragmentation functions as

$$f_{\gamma q(\bar{q})}(x,M)=\frac{\alpha}{2\pi}\ln\left[\frac{M^2}{\Lambda_{\rm QCD}^2}\right]\times\left[\frac{\hat{e}_{q(\bar{q})}^2(2.21-1.28x+1.29x^2)x^{-0.951}}{1-1.63\ln(1-x)}+0.002(1-x)^{2.0}x^{-2.54}\right]$$
$$f_{\gamma g}(x,M)=\frac{\alpha}{2\pi}\ln\left[\frac{M^2}{\Lambda_{\rm QCD}^2}\right]0.0243(1-x)^{1.03}x^{-1.97}\,, \tag{2.4}$$

where $\hat{e}_{q(\bar{q})}$ denotes the charge of the outgoing quark (antiquark) $q(\bar{q})$ in units of e, M is the mass factorization scale, and the running electromagnetic fine structure constant is $\alpha=e^2(\mu^2)/4\pi$.

TABLE I. Results for the partial hadronic cross sections (in pb) for the two-body inclusive reaction $p+\bar{p}\rightarrow W^+ +\gamma+X$ in the $q\bar{q}$ channel at $\sqrt{S}=1.8$ TeV.

r	0.50	1.0	2.0
α_S	0.145	0.129	0.116
$\sigma_{q\bar{q}}^{\rm Born}$	2.66	2.62	2.58
$\sigma_{\rm SV}^{P}$	0.31	0.51	0.67
$\sigma_{\rm Ia,1}$	0.02	0.02	0.02
$\sigma_{\rm Ia,2}$	0.05	−0.05	−0.11
$\sigma_{\rm Ia,3}$	−18.45	−18.25	−17.98
$\sigma_{\rm Ia}$	−18.39	−18.28	−18.07
$\sigma_{\rm Ib,1}$	0.02	0.02	0.01
$\sigma_{\rm Ib,2}$	0.04	−0.04	−0.10
$\sigma_{\rm Ib,3}$	−18.43	−18.23	−17.94
$\sigma_{\rm Ib}$	−18.38	−18.25	−18.03
$\sigma_{I,4}$	37.20	36.83	36.29
$\sigma_{f,1,1,a}$	0.07	0.06	0.05
$\sigma_{f,1,2,a}$	1.41	1.20	1.04
$\sigma_{f,1,3,a}$	−1.30	−1.12	−0.97
$\sigma_{f,1,1,b}$	0.08	0.07	0.06
$\sigma_{f,1,2,b}$	1.20	1.03	0.90
$\sigma_{f,1,3,b}$	−1.14	−0.98	−0.85
$\sigma_{f,2,1,a}$	1.12	0.98	0.87
$\sigma_{f,2,2,a}$	28.97	26.45	23.44
$\sigma_{f,2,3,a}$	−29.03	−26.51	−23.50
$\sigma_{f,2,1,b}$	1.12	0.99	0.87
$\sigma_{f,2,2,b}$	29.95	26.31	23.33
$\sigma_{f,2,3,b}$	−30.01	−26.37	−23.38
$\sigma_{f,3}$	−2.30	−2.02	−1.79
$\sigma_{q\bar{q}({\rm finite})}^{P}$	0.16	0.10	0.07
$\sigma_{q\bar{q}({\rm brems})}$	0.003	0.003	0.003
$\sigma_{q\bar{q}({\rm error})}$	$\sim(10^{-4})$	$\sim(10^{-4})$	$\sim(10^{-4})$
$\sigma_{q\bar{q}}$	3.61	3.52	3.52

TABLE II. Results for the partial hadronic cross sections (in pb) for the two-body inclusive reaction $p+\bar{p}\rightarrow W^+ +\gamma+X$ in the qg channel at $\sqrt{S}=1.8$ TeV.

r	0.50	1.0	2.0
α_S	0.145	0.129	0.116
$\sigma_{qg,f,1}^{\rm I}$	0.38	0.31	0.26
$\sigma_{qg,f,2}^{\rm I}$	0.78	0.66	0.56
$\sigma_{qg,f,3}^{\rm I}$	−0.80	−0.67	−0.57
$\sigma_{qg,{\rm finite}}^{P,{\rm I}}$	0.38	0.31	0.26
$\sigma_{qg}^{\rm I,col}$	−0.22	−0.25	−0.26
$\sigma_{qg,f,1}^{\rm II}$	0.12	0.10	0.09
$\sigma_{qg,f,2}^{\rm II}$	0.15	0.13	0.11
$\sigma_{qg,f,3}^{\rm II}$	−0.08	−0.07	−0.06
$\sigma_{qg,{\rm finite}}^{P,{\rm II}}$	0.19	0.16	0.13
$\sigma_{qg}^{\rm II,col}$	−0.04	−0.04	−0.04
$\tilde{\sigma}_{qg}^{P}$	0.15	0.12	0.10
$\sigma_{qg({\rm brems})}$	0.02	0.02	0.02
$\sigma_{qg({\rm error})}$	$\sim(10^{-9})$	$\sim(10^{-9})$	$\sim(10^{-9})$
σ_{qg}	0.48	0.33	0.21

B. Total cross section for the two-body inclusive reaction $p+\bar{p}\rightarrow W^+ +\gamma+X$

All terms in expressions (2.2) and (2.3) will produce nonvanishing contributions in this scenario. In Table I we show the results for the $q\bar{q}$ channel cross sections in pb at the three scales $r=0.5$, 1.0, and 2.0, where $r=M/M_W=\mu/M_W$ and M,μ are the mass factorization and renormalization scales, respectively. The second entry of Table I shows the value used for α_S at these scales. In all our runs we use $\alpha=1/137.036$ for the fine structure constant and $G_F=1.166\,39\times10^{-5}$ GeV^{-2} for the Fermi coupling constant.

The corresponding results for the qg channel contributions to the two-body inclusive hadronic reaction $p+\bar{p}\rightarrow W^+ +\gamma+X$ are summarized in Table II. Finally,

TABLE III. Results for the partial hadronic cross sections (in pb) for the two-body inclusive reaction $p+\bar{p}\rightarrow W^+ +\gamma+X$ in the $g\bar{q}$ channel at $\sqrt{S}=1.8$ TeV.

r	0.50	1.0	2.0
α_S	0.145	0.129	0.116
$\sigma_{g\bar{q},f,1}^{\rm I}$	0.14	0.12	0.10
$\sigma_{g\bar{q},f,2}^{\rm I}$	0.60	0.50	0.42
$\sigma_{g\bar{q},f,3}^{\rm I}$	−0.61	−0.51	−0.43
$\sigma_{g\bar{q},{\rm finite}}^{P,{\rm I}}$	0.13	0.11	0.09
$\sigma_{g\bar{q}}^{\rm I,col}$	−0.18	−0.20	−0.20
$\sigma_{g\bar{q},f,1}^{\rm II}$	0.38	0.31	0.26
$\sigma_{g\bar{q},f,2}^{\rm II}$	0.48	0.40	0.34
$\sigma_{g\bar{q},f,3}^{\rm II}$	−0.27	−0.23	−0.20
$\sigma_{g\bar{q},{\rm finite}}^{P,{\rm II}}$	0.59	0.49	0.41
$\sigma_{g\bar{q}}^{\rm II,col}$	−0.13	−0.13	−0.13
$\tilde{\sigma}_{g\bar{q}}^{P}$	0.11	0.09	0.07
$\sigma_{g\bar{q}({\rm brems})}$	0.08	0.08	0.07
$\sigma_{g\bar{q}({\rm error})}$	$\sim(10^{-8})$	$\sim(10^{-8})$	$\sim(10^{-8})$
$\sigma_{g\bar{q}}$	0.61	0.43	0.31

the corresponding results for the $g\bar{q}$ channel are summarized in Table III.

We thus obtain total cross sections for the two-body inclusive reaction $p+\bar{p}\rightarrow W^{+}+\gamma+X$ of 4.70, 4.28, and 4.04 pb for $r=0.5$, 1.0, and 2.0, respectively. The total cross section at order α_S is thus a decreasing function of the scale r, confirming the results obtained in a previous study [7]. The strong dependence of the cross section on the scale r means that order α_S^2 corrections are large and they must be included for accurate predictions in this scenario. This was also pointed out in [7] when studying the single particle photon inclusive cross section.

If we compare these results with the ones previously reported for the single particle inclusive total cross section in [7], we note a considerable reduction of the total cross section in the present calculation. The smaller values can be attributed to a larger cut in the photon angle and the effect of experimental cuts on the W^+ boson, which was treated previously in an inclusive fashion.

We also note that in the approximation we are using here the bremsstrahlung contributions are negligible in the $q\bar{q}$ channel and that their contribution in the other channels amounts to not more than 2% of the total cross section. This would make big deviations from the leading logarithm bremsstrahlung approximation easy to study.

The next to last rows in Tables I, II, and III show that the errors introduced by the Δ_x, Δ_y, and Δ_v cuts (see Sec. V of [1]), are negligible, and thus our prescription for splitting the x, y, and v integrals when adding up the histograms in consistent.

C. Total cross sections of $p+\bar{p}\rightarrow W^{+}+\gamma+\text{jet}$ and $p+\bar{p}\rightarrow W^{+}+\gamma$

With the choice of parameters x_0, y_0, and v_0 explained in Sec. I, the only terms in (2.2) contributing to the reaction $p+\bar{p}\rightarrow W^{+}+\gamma+\text{jet}$ are

$$\begin{aligned}\sigma_{q\bar{q}}&=\sigma_{f,1,1,\mathrm{a}}+\sigma_{f,1,1,\mathrm{b}}\,,\\ \sigma_{qg}&=\sigma^{\mathrm{I}}_{qg,f,1}+\sigma^{\mathrm{II}}_{qg,f,1}+\tilde{\sigma}^{P}_{qg}\,,\\ \sigma_{g\bar{q}}&=\sigma^{\mathrm{I}}_{g\bar{q},f,1}+\sigma^{\mathrm{II}}_{g\bar{q},f,1}+\tilde{\sigma}^{P}_{g\bar{q}}\,.\end{aligned}\tag{2.5}$$

TABLE IV. Results for the partial and total hadronic cross sections (in pb) for the reaction $p+\bar{p}\rightarrow W^{+}+\gamma+\text{jet}$ at $\sqrt{S}=1.8$ TeV.

r	0.50	1.0	2.0
α_S	0.145	0.129	0.116
$\sigma_{f,1,1,\mathrm{a}}$	0.54	0.46	0.39
$\sigma_{f,1,1,\mathrm{b}}$	0.52	0.44	0.38
$\sigma_{q\bar{q}}$	1.05	0.89	0.77
$\sigma^{\mathrm{I}}_{qg,f,1}$	0.26	0.21	0.17
$\sigma^{\mathrm{II}}_{qg,f,1}$	0.14	0.11	0.09
$\tilde{\sigma}^{P}_{qg}$	0.12	0.10	0.08
σ_{qg}	0.52	0.42	0.35
$\sigma^{\mathrm{I}}_{g\bar{q},f,1}$	0.07	0.06	0.05
$\sigma^{\mathrm{II}}_{g\bar{q},f,1}$	0.41	0.33	0.27
$\tilde{\sigma}^{P}_{g\bar{q}}$	0.10	0.08	0.06
$\sigma_{g\bar{q}}$	0.58	0.47	0.39
σ_{total}	2.15	1.79	1.51

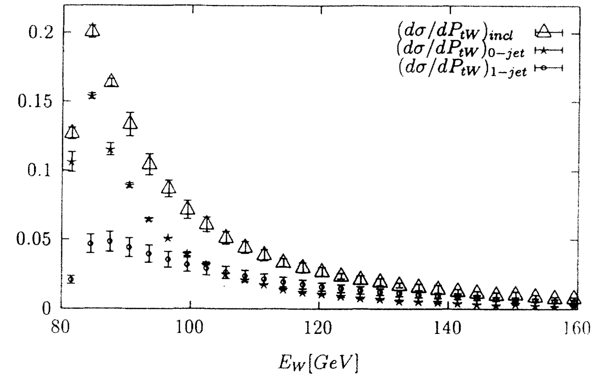

FIG. 1. Differential cross section $d\sigma/dE_W$ (pb/GeV).

The results for the contributions of all these terms to the hadronic cross section are shown in Table IV for the three scales $r=0.5$, 1.0, and 2.0. At these scales we thus obtain for the total cross sections of the one-jet reaction values of 2.15, 1.79, and 1.51 pb, respectively. As in the two-body inclusive case, the variation is large in the one-jet scenario so we need to include higher order QCD corrections to make more accurate predictions. Unfortunately, these higher order corrections are not available.

Subtracting the above numbers from the ones for the two-body inclusive reaction $p+\bar{p}\rightarrow W^{+}+\gamma+X$ we obtain for the zero-jet reaction $p+\bar{p}\rightarrow W^{+}+\gamma$ the values of 2.55, 2.50, and 2.53 pb at the scales $r=0.5$, 1.0, and 2.0, respectively. In this scenario we do not need to include order α_S^2 QCD corrections to make our predictions more reliable, since they are already very stable.

III. SINGLE DIFFERENTIAL CROSS SECTIONS AND CORRELATIONS

We now turn to analysis of the single differential distributions and correlations. Our results are shown in Figs. 1–25. The error bars represent the theoretical uncertainty associated with the dependence of our results on the mass factorization and renormalization scales. They have been obtained evaluating the distributions at the two scales $r=0.5$ and 2.0. Note that the central values and the upper and lower limits still contain a numerical error introduced via the Monte carlo simulation. This er-

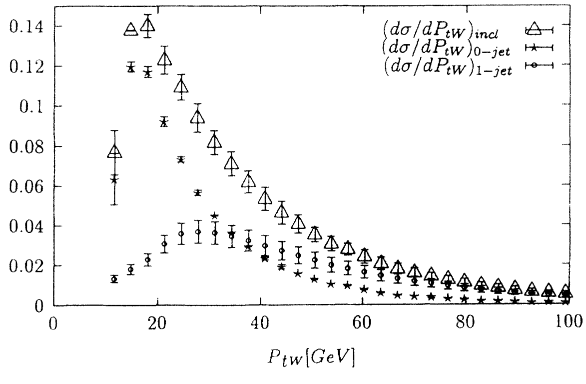

FIG. 2. Differential cross section $d\sigma/dP_{tW}$ (pb/GeV).

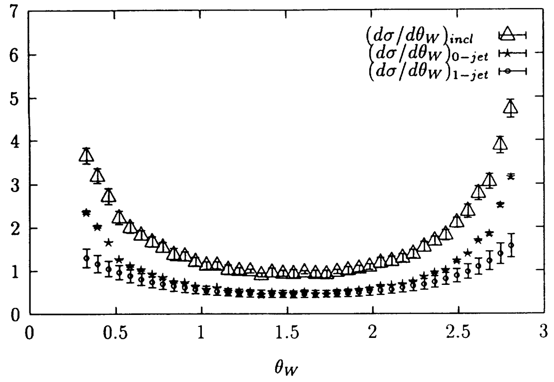

FIG. 3. Differential cross section $d\sigma/d\theta_W$ (pb/rad).

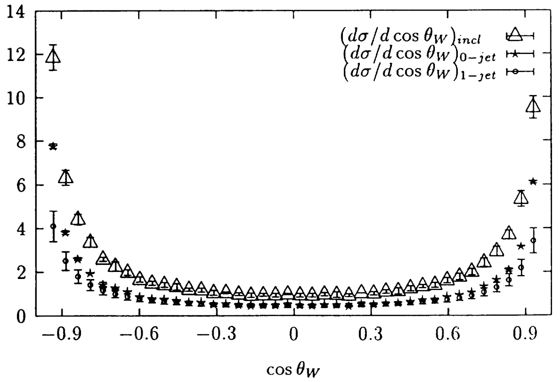

FIG. 4. Differential cross section $d\sigma/d\cos\theta_W$ (pb).

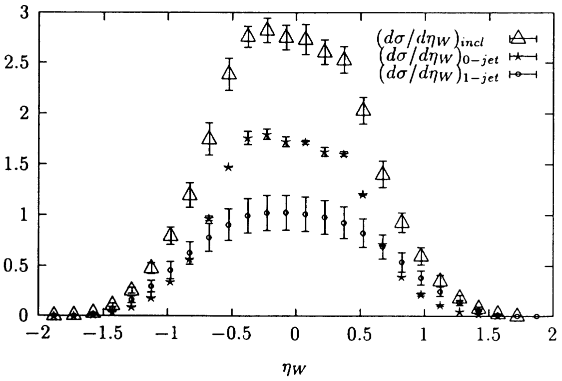

FIG. 5. Differential cross section $d\sigma/d\eta_W$ (pb).

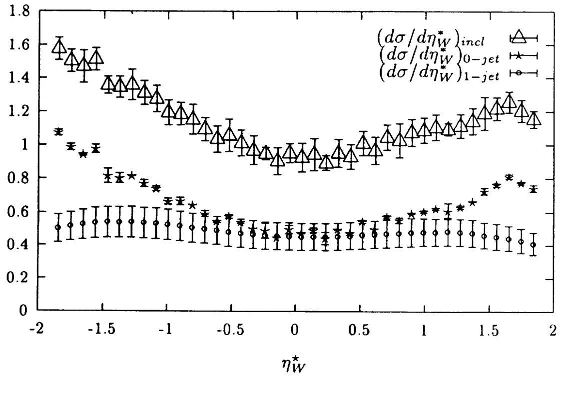

FIG. 6. Differential cross section $d\sigma/d\eta_W^{*}$ (pb).

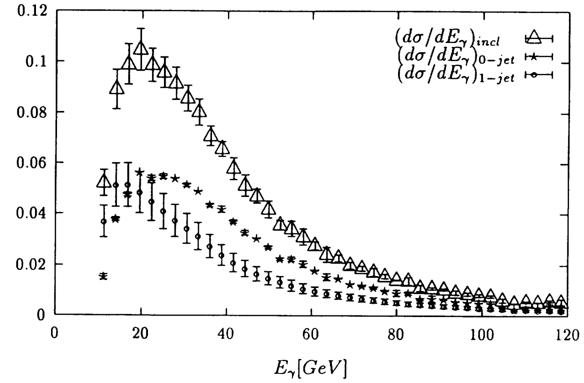

FIG. 7. Differential cross section $d\sigma/dE_\gamma$ (pb/GeV).

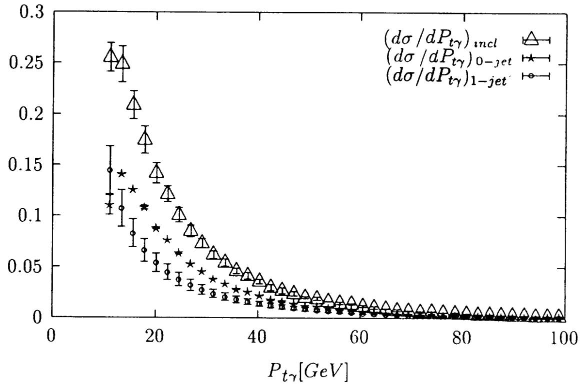

FIG. 8. Differential cross section $d\sigma/dP_{t\gamma}$ (pb/GeV).

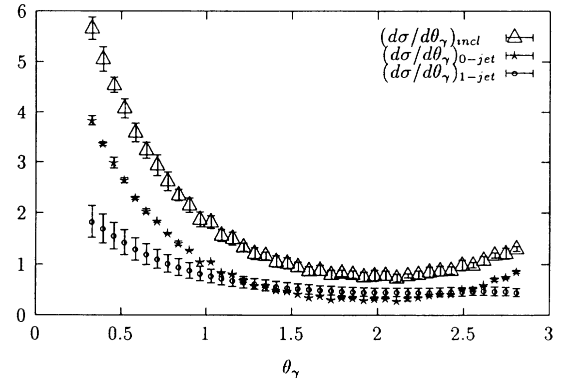

FIG. 9. Differential cross section $d\sigma/d\theta_\gamma$ (pb/rad).

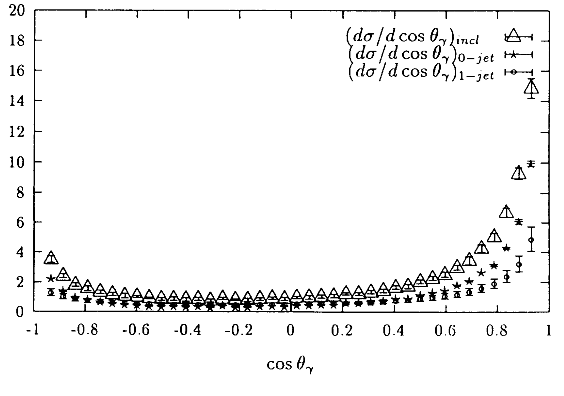

FIG. 10. Differential cross section $d\sigma/d\cos\theta_\gamma$ (pb).

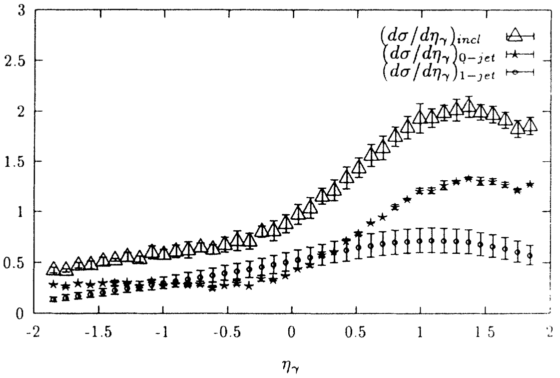

FIG. 11. Differential cross section $d\sigma/d\eta_\gamma$ (pb).

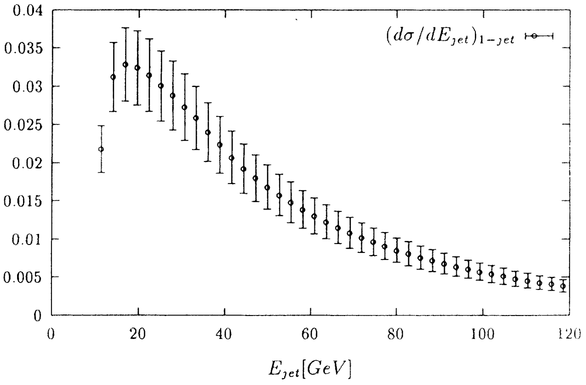

FIG. 12. Differential cross section $d\sigma/dE_{\rm jet}$ (pb/GeV).

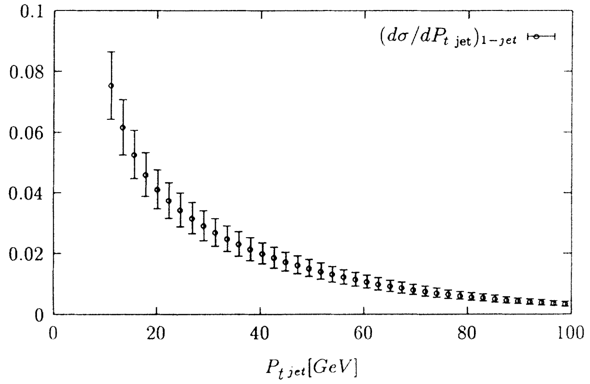

FIG. 13. Differential cross section $d\sigma/dP_{t\ \rm jet}$ (pb/GeV).

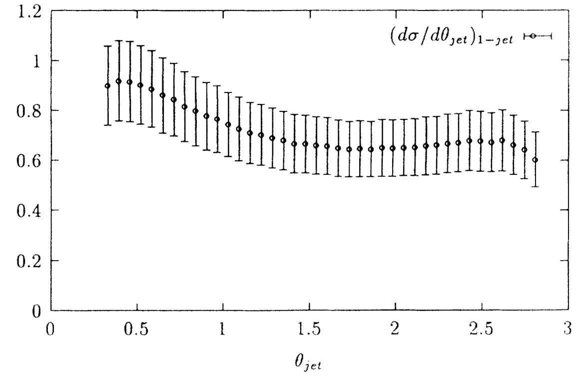

FIG. 14. Differential cross section $d\sigma/d\theta_{\rm jet}$ (pb/rad).

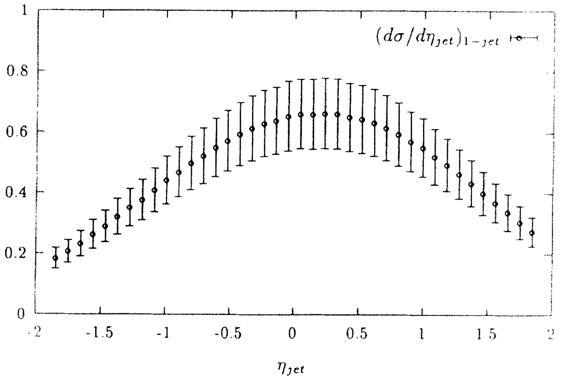

FIG. 15. Differential cross section $d\sigma/d\eta_{\rm jet}$ (pb).

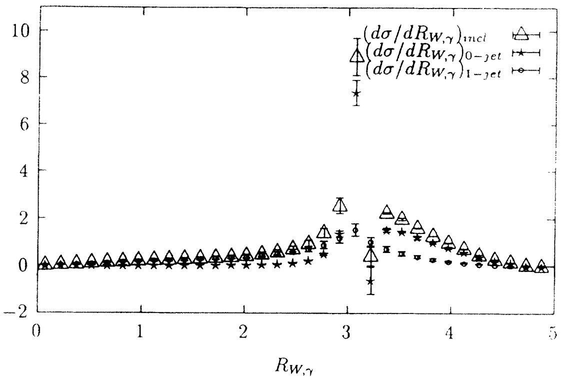

FIG. 16. Differential cross section $d\sigma/dR_{W,\gamma}$ (pb).

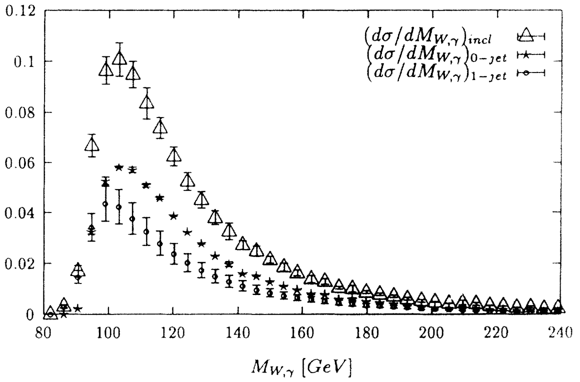

FIG. 17. Differential cross section $d\sigma/dM_{W,\gamma}$ (pb/GeV).

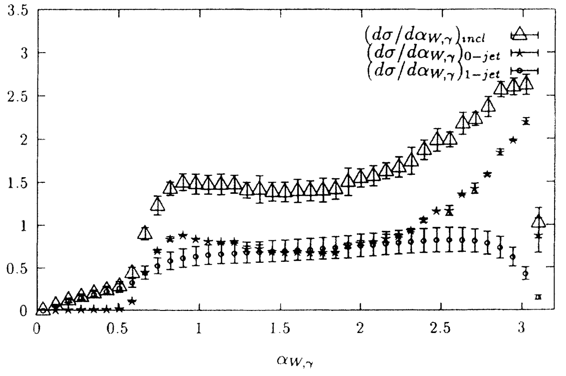

FIG. 18. Differential cross section $d\sigma/d\alpha_{W,\gamma}$ (pb/rad).

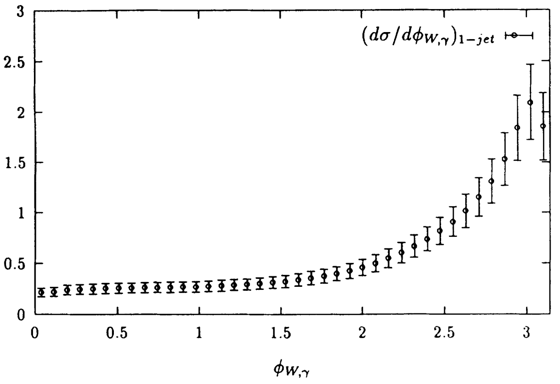

FIG. 19. Differential cross section $d\sigma/d\phi_{W,\gamma}$ (pb/rad).

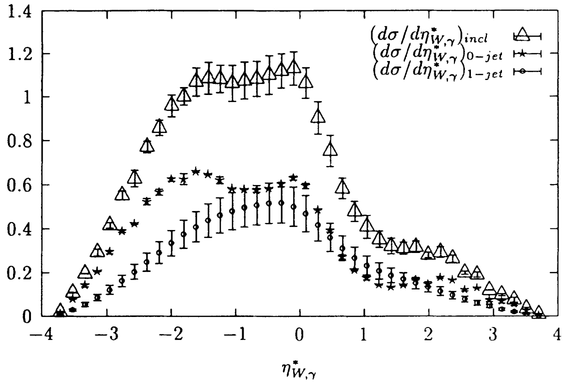

FIG. 20. Differential cross section $d\sigma/d\eta^*_{W,\gamma}$ (pb).

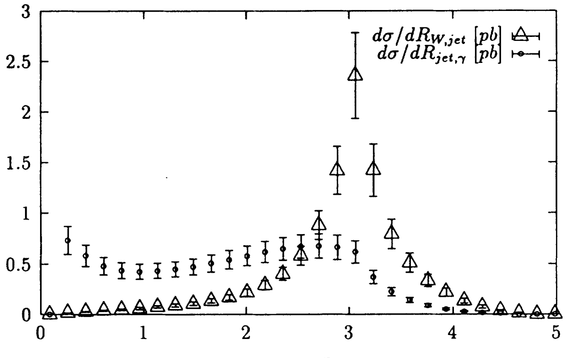

FIG. 21. Differential cross sections $d\sigma/dR_{W,\rm jet}$ (pb) and $d\sigma/dR_{\rm jet,\gamma}$ (pb).

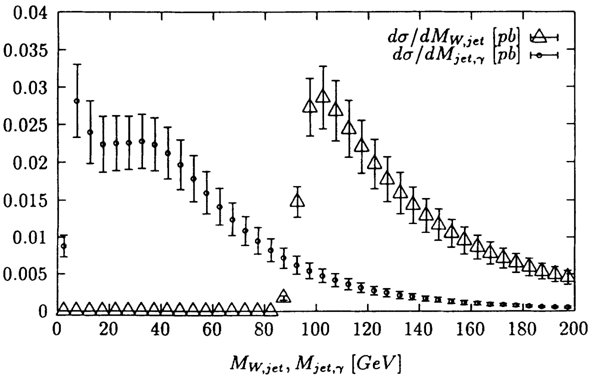

FIG. 22. Differential cross sections $d\sigma/dM_{W,\rm jet}$ (pb/GeV) and $d\sigma/dM_{\rm jet,\gamma}$ (pb/GeV).

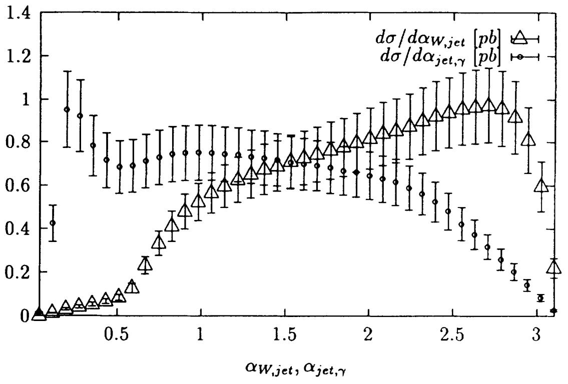

FIG. 23. Differential cross sections $d\sigma/d\alpha_{W,\rm jet}$ (pb/rad) and $d\sigma/d\alpha_{\rm jet,\gamma}$ (pb/rad).

ror is negligible in our one-jet results but it is larger in our two-body inclusive and zero-jet results. Regions with big error bars in our plots may be interpreted as regions where perturbation theory at order α_S is not reliable and thus higher order QCD corrections would be needed to make more accurate theoretical predictions.

In general, the single differential distributions and correlations have very little dependence on the scale r in the scenario where the W^+ and photon are produced with zero outgoing jets. If we include one-jet processes we increase the statistics by more than 60%, but a non-negligible theoretical uncertainty is introduced by the scale dependence of the one-jet processes. To make theoretical predictions for single distributions and correlations more reliable in the two-body inclusive scenario, we would thus need to include the order α_S^2 corrections.

Figures 1–6 show results for single differential distributions for the W^+ boson and Figs. 7–11 show the corresponding photon distributions. These plots demonstrate that the W boson is mainly concentrated in the regions of small energy and transverse momentum in all three scenarios. In the one-jet scenario E_W peaks at around 85 GeV (Fig. 1) while P_{tW} peaks at around 30 GeV (Fig. 2). In the other two scenarios the single differential distributions of E_W and P_{tW} are monotonical-

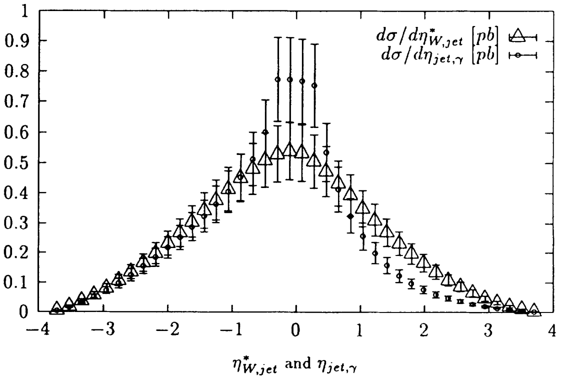

FIG. 24. Differential cross sections $d\sigma/d\eta^*_{W,\rm jet}$ (pb) and $d\sigma/d\eta_{\rm jet,\gamma}$ (pb).

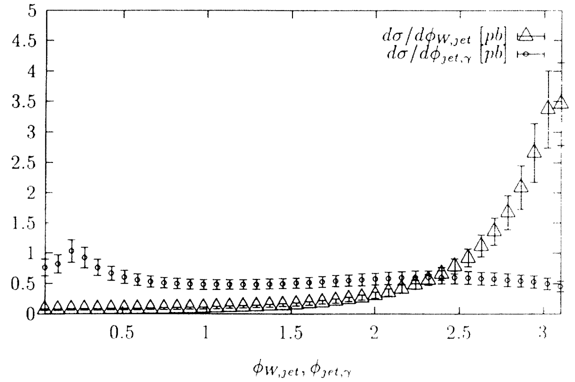

FIG. 25. Differential cross sections $d\sigma/d\phi_{W,\mathrm{jet}}$ (pb) and $d\sigma/d\phi_{\mathrm{jet},\gamma}$ (pb/rad).

ly decreasing functions except for the physical and experimental lower cuts.

Figures 3, 4, and 6 show clearly that there are dips in the polar angle and pseudorapidity distributions of the W boson at around $\theta_W=\pi/2$ in the zero-jet and two-body inclusive scenarios, with smooth dips at around the same point in the one-jet scenario. This is very different to what we observe for the photon polar angle and rapidity distributions, which present dips at around $\theta_W=2\pi/3$ in the zero-jet scenario only (Figs. 9, 10, and 11).

The zero-jet scenario would so far be the best for studying deviations from the standard model by looking at photon distributions, since on the one hand the theoretical uncertainties related to dependences on the scale r are small and on the other hand the two- to three-body contributions are suppressed so that the partonic zeros still show up as wide dips in the angular and rapidity distributions of the photon (see Figs. 9, 10, and 11). The θ_γ distribution maintains its features when one-jet events are added, as seen in Fig. 9; however, the dip in rapidity is smeared out, as seen in Fig. 11. If photon bremsstrahlung contributions are not well accounted for by the leading logarithm approximation, these may disturb the dips in the photon angle and the photon rapidity and all other photon single and double differential distributions and correlations in the zero-jet scenario. Therefore, to isolate this effect it may be important to look also at physical quantities in the one-jet scenario, where there is no contribution from photon bremsstrahlung at present order in perturbation theory.

Figures 12–15 show single differential distributions of the outgoing jet in the one-jet scenario. We see that the jet is concentrated in the low energy, low P_t, and central rapidity regions. We also note that the scale dependence increases in these regions. The plot in Fig. 14 shows a quite uniform polar angle distribution for the jet.

Figures 16–25 summarize our results for single correlations between outgoing pairs of particles. The same comments about the scale dependences in the different scenarios observed in Figs. 1–15 are valid here.

The $R_{W,\gamma}$ cone size correlation in Fig. 16 presents a sharp peak followed by a sharp dip that falls below zero near $R_{W,\gamma}=\pi$ in the zero-jet and two-body inclusive scenarios. A similar feature was observed by Mangano, Nason, and Ridolfi [8] in $R_{q,\bar{q}}$ for heavy quark pair correlations with fixed quark rapidity. The corresponding correlation in the one-jet process presents no anomalous behavior, suggesting that the observed dips in the other two scenarios are the effect of the subtraction pieces introduced when the factorization theorem is implemented to cancel collinear singularities associated with untagged jets produced parallel to the beams.

The $R_{W,\mathrm{jet}}$ cone size correlation in Fig. 21 has a very symmetric shape with a peak centered at π. On the other hand, $R_{\mathrm{jet},\gamma}$ in Fig. 21 is much smoother between 0.2 and π, falling rapidly to zero outside this range. This means that the jet and the photon are approximately uncorrelated in cone size; however, the jet and the W boson are highly correlated. Figure 25 confirms that the latter pair of particles are mainly concentrated on a plane that contains the beams, i.e., the distribution of the azimuthal angle difference $\phi_{W,\mathrm{jet}}$ peaks at π. However, $\phi_{\mathrm{jet},\gamma}$ is approximately flat over the whole range. The observed bump near $\phi_{\mathrm{jet},\gamma}=R_{\mathrm{jet},\gamma}=0.2$ is caused by the required experimental cut on the cone size.

Pair mass correlations are of interest when studying deviations from the standard model, as pointed out in [6]. The pair mass correlations $M_{W,j}=\sqrt{(Q_1+p_j)^2}$ with $j=\gamma$,jet in Figs. 17 and 22 both peak at around 100 GeV; however, the correlation $M_{\mathrm{jet},\gamma}$ has a plateau between 20 and 40 GeV, slowly falling to zero above 40 GeV.

Figures 18 and 23 show the distributions of the angles $\alpha_{i,j}$ between pairs of particles i,j. As expected $\alpha_{W,\gamma}$ peaks near $\alpha=\pi$ in the zero-jet scenario, since here the main contributions come from back to back two- to two-body partonic reactions. The smearing is introduced when boosting the partonic system into the hadronic system. This is not the case for the corresponding correlation in the one-jet scenario, which shows that the W boson and the photon are uncorrelated in the angle difference. The angular correlations between the jet and the W or the photon are also quite smooth.

Since transverse momenta are preserved under Lorentz boosts along the beamline, the distribution of the azimuthal angle difference $\phi_{W,\gamma}$ only makes sense in the one-jet scenario, which is shown in Fig. 19. It also peaks at around $\phi_{W,\gamma}=\pi$, meaning that the W and the photon are mainly concentrated on the plane that contains the beams. This, along with the information contained in Fig. 25, shows that the beams and the three particles produced in the one-jet scenario are approximately coplanar.

Figure 20 shows the distributions of the pseudorapidity difference between the W and the photon in the three scenarios. In all cases the events are concentrated along the negative region, which means that the photon is produced with an angle with respect to the incoming antiproton beam that is usually smaller than the corresponding angle of the W boson. We note the presence of two dips in the zero-jet scenario, one around $\eta^*_{W,\gamma}=-1$ and the other around $\eta^*_{W,\gamma}=1.3$. These dips are smeared into plateaus in the inclusive scenario by the effect of one-jet processes. In Fig. 24 we see a very different behavior for the pseudorapidity differences of jet and W

or photon: $\eta^*_{W,\text{jet}}$ is symmetric around 0 while $\eta^*_{\text{jet},\gamma}$ receives bigger contributions on the negative axis but both correlations peak at 0.

IV. DOUBLE DIFFERENTIAL CROSS SECTIONS AND CORRELATIONS

Double differential cross sections and correlations help us visualize the qualitative features of the spatial distributions of particles hitting an experimental detector. We present in Figs. 26(a)–45 results obtained by averaging Monte Carlo runs at $r=0.5$ and $r=2.0$. Figures 26(a)–27(c) correspond to double differential distributions of the W, while Figs. 28(a)–29(c) show the corresponding double differential distributions of the photon. Figures 30(a)–34(c) contain the plots of the correlations between the W boson and the photon, and Figs. 35–45 the various correlations between the jet and either the W or the photon.

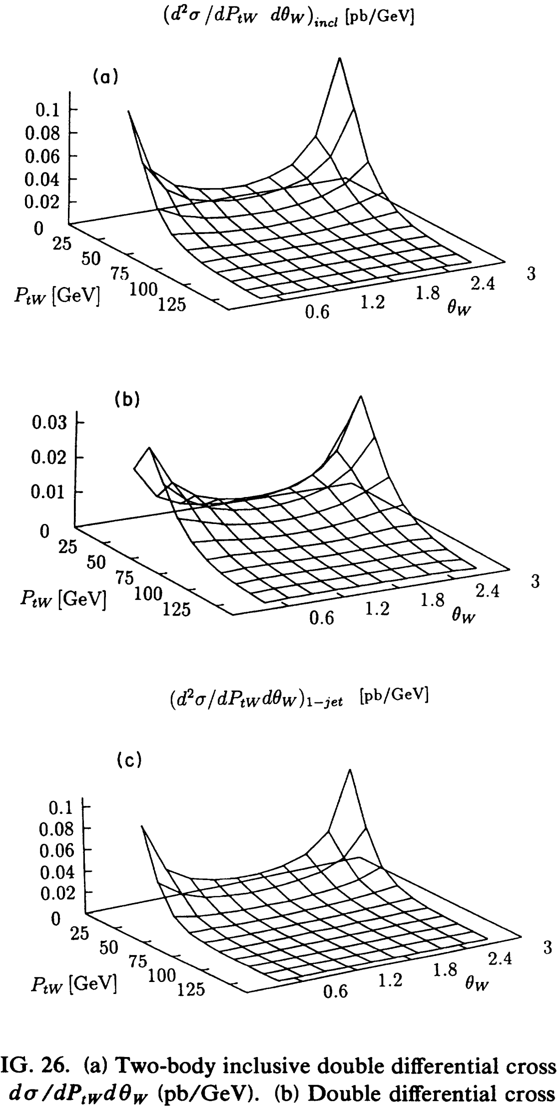

FIG. 26. (a) Two-body inclusive double differential cross section $d\sigma/dP_{tW}d\theta_W$ (pb/GeV). (b) Double differential cross section $d\sigma/dP_{tW}d\theta_W$ (pb/GeV) for the one-jet process. (c) Double differential cross section $d\sigma/dP_{tW}d\theta_W$ (pb/GeV) for the zero-jet process.

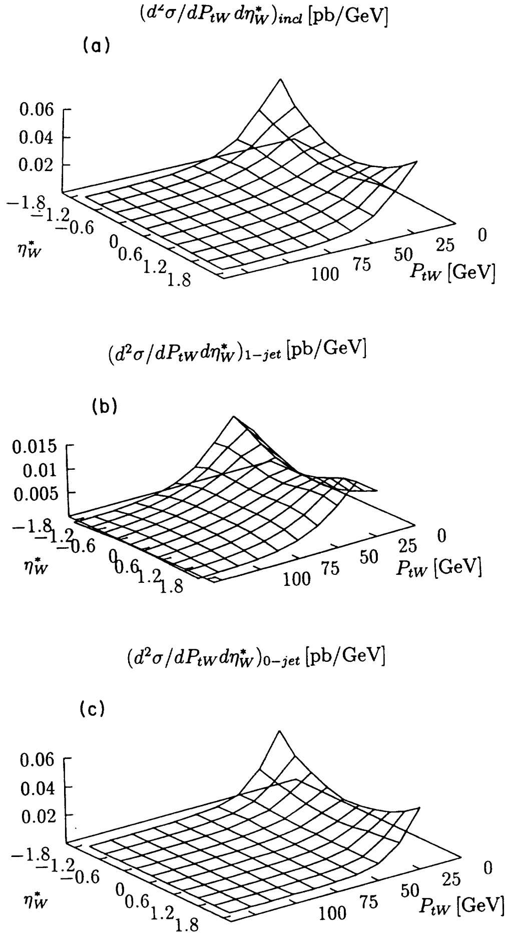

FIG. 27. (a) Two-body inclusive double differential cross section $d\sigma/dP_{tW}d\eta^*_W$ (pb/GeV). (b) Double differential cross section $d\sigma/dP_{tW}d\eta^*_W$ (pb/GeV) for the one-jet process. (c) Double differential cross section $d\sigma/dP_{tW}d\eta^*_W$ (pb/GeV) for the zero-jet process.

First we look at the double differential distributions of P_t vs θ for the W boson [Figs. 26(a), 26(b), and 26(c)]. We conclude that the dip in θ_W, already observed in the single differential distribution (Fig. 3), increases in relative depth as P_{tW} decreases. In the one-jet scenario the double differential distribution clearly peaks along the line $P_{tW}=30$ GeV for all values of θ_W [Fig. 26(b)]. In the other two scenarios the peaks move down to small values of P_{tW}, but in Figs. 26(a) and 26(c) they are not clearly seen due to the low density of bins that has been used on each axis; these peaks show up in the single differential distributions in Fig. 2, however, where the density of bins is four times bigger. Similar conclusions are obtained when looking at P_t vs pseudorapidity for the W in Figs. 27(a), 27(b), and 27(c).

The corresponding double differential distributions for the photon have been plotted in Figs. 28(a)–29(c). The effect of the one-jet processes on the dips in angle and rapidity which reflect the partonic zeros is clearly visible in these figures. We note that in the zero-jet scenario the dips increase their relative depth as $P_{t\gamma}$ decreases. This

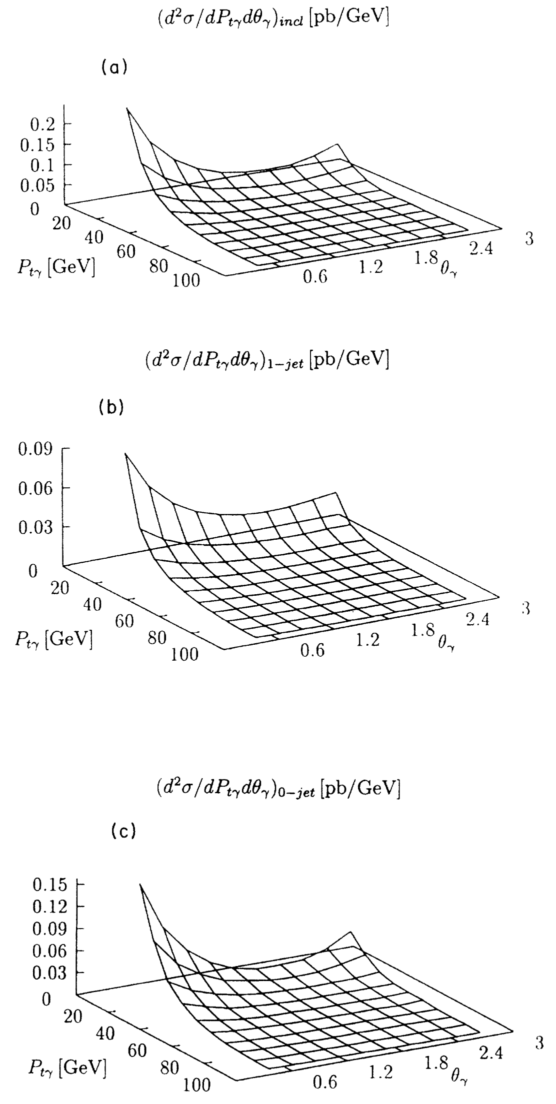

FIG. 28. (a) Two-body inclusive double differential cross section $d\sigma/dP_{t\gamma}d\theta_\gamma$ (pb/GeV). (b) Double differential cross section $d\sigma/dP_{t\gamma}d\theta_\gamma$ (pb/GeV) for the one-jet process. (c) Double differential cross section $d\sigma/dP_{t\gamma}d\theta_\gamma$ (pb/GeV) for the zero jet process.

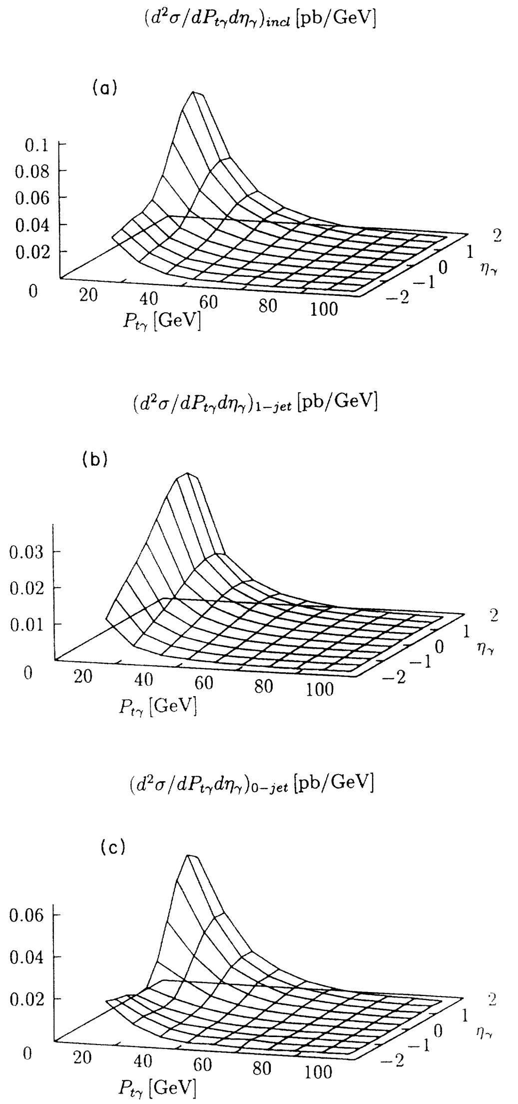

FIG. 29. (a) Two-body inclusive double differential cross section $d\sigma/dP_{t\gamma}d\eta_\gamma$ (pb/GeV). (b) Double differential cross section $d\sigma/dP_{t\gamma}d\eta_\gamma$ (pb/GeV) for the one-jet process. (c) Double differential cross section $d\sigma/dP_{t\gamma}d\eta_\gamma$ (pb/GeV) for the zero-jet process.

suggests that the effects of deviations from the standard model on the single differential distributions in the polar angle and rapidity of photon would be enhanced if $P_{t\gamma}$ were constrained to take values below a certain bound, say 25 GeV.

From the results in the previous subsection we already know that the events are mainly concentrated in the regions of small E_W and small E_γ. Moreover, Figs. 30(a), 30(b), and 30(c) show that E_W and E_γ are not very correlated and that the bulk of the events is always in the small $E_W(\gamma)$ region, regardless of the value of $E_\gamma(W)$. The peak in the double differential cross section is steepest in the zero-jet scenario, however [see Fig. 30(c)].

Since P_t is conserved under Lorentz boosts along the beams, the W and the photon are exactly correlated in transverse momentum space in the zero-jet scenario (i.e., $P_{tW}=P_{t\gamma}$), so this correlation only makes sense in the one-jet scenario, where it gets smeared and it peaks around the line $P_{tW}=30$ GeV regardless of the value of $P_{t\gamma}$ (see Fig. 31).

The pseudorapidity correlation between W and γ clearly shows the effect of the partonic zero, as we can appreciate in Fig. 32(c) in the zero-jet scenario. The double differential cross section shows a valley in the negative η_γ region along the whole range of η_W^*. Inclusion of one-jet processes [see Fig. 32(b)] would push the valley up producing a plateau instead, as seen in Fig. 32(a) for the two-body inclusive scenario and smearing out the dip in the single distribution, as already noted in Fig. 11.

Due to the exact correlation between P_{tW} and $P_{t\gamma}$ in

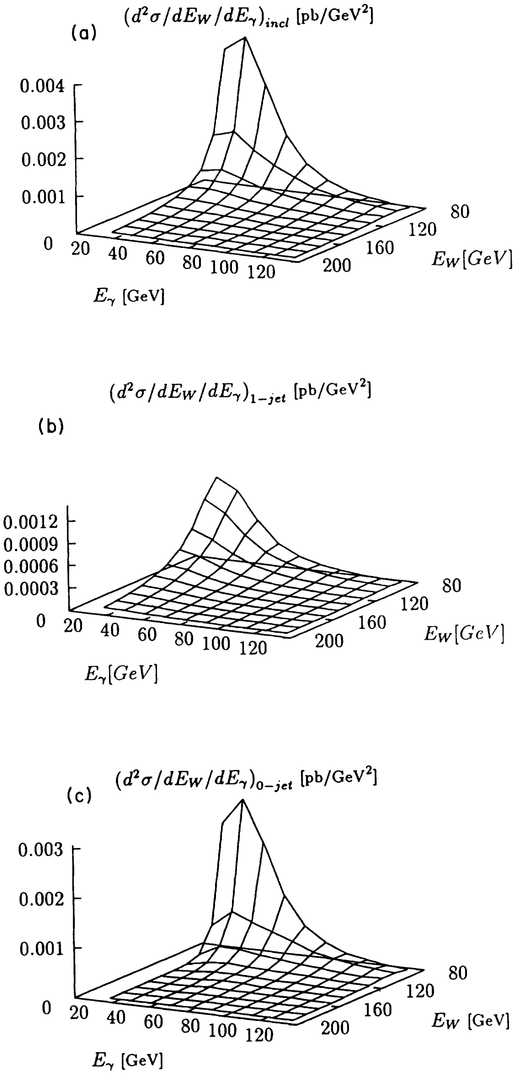

FIG. 30. (a) Two-body inclusive double differential cross section $d\sigma/dE_W dE_\gamma$ (pb/GeV^2). (b) Double differential cross section $d\sigma/dE_W dE_\gamma$ (pb/GeV^2) for the one-jet process. (c) Double differential cross section $d\sigma/dE_W dE_\gamma$ (pb/GeV^2) for the zero-jet process.

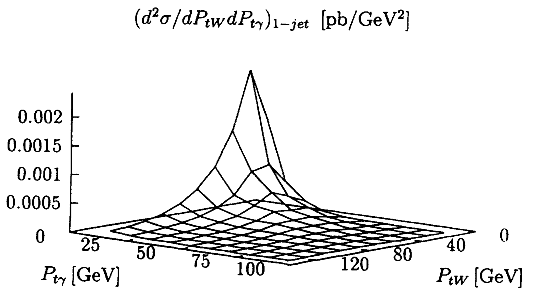

FIG. 31. Double differential cross section $d\sigma/dP_{tW}dP_{t\gamma}$ (pb/GeV^2) for the one-jet process.

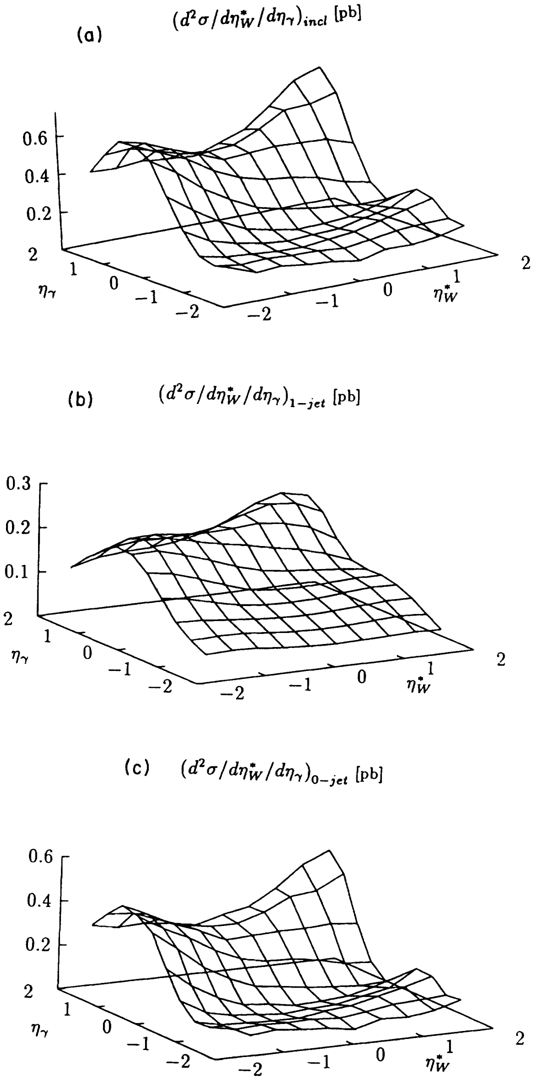

FIG. 32. (a) Two-body inclusive double differential cross section $d\sigma/d\eta_W^* d\eta_\gamma$ (pb). (b) Double differential cross section $d\sigma/d\eta_W^* d\eta_\gamma$ (pb) for the one-jet process. (c) Double differential cross section $d\sigma/d\eta_W^* d\eta_\gamma$ (pb) for the zero-jet process.

the zero-jet scenario, the correlation between P_{tW} and η_γ in the zero-jet scenario [Fig. 33(c)] looks similar to the double differential distribution of $P_{t\gamma}$ vs η_γ [Fig. 29(c)], i.e., it shows an increasing effect of the partonic zero as P_{tW} decreases so that the photon rapidity dip becomes relatively deeper at small P_{tW}. One-jet processes present no dip in this double correlation, as seen in Fig. 33(b), and their effect when looking at the two-body inclusive process in Fig. 33(a) is to smear out the dip, which reappears below $P_{tW}=30$ GeV.

The pseudorapidity of the W shows dips in all three scenarios (Fig. 6) and these dips are enhanced if $P_{t\gamma}$ is constrained to be smaller than 30 GeV, as inferred from Figs. 34(a), 34(b), and 34(c). We contrast this with the results for the rapidity of the photon, which only shows a clear dip in the zero-jet scenario, even when looking at

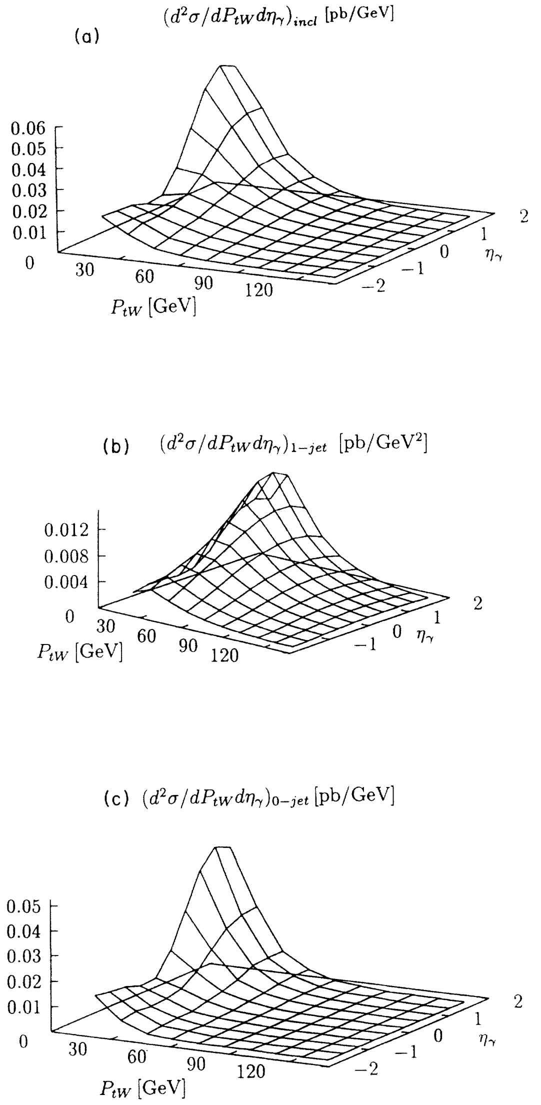

FIG. 33. (a) Two-body inclusive double differential cross section $d\sigma/dP_{tW}d\eta_\gamma$ (pb/GeV). (b) Double differential cross section $d\sigma/dP_{tW}d\eta_\gamma$ (pb/GeV) for the one-jet process. (c) Double differential cross section $d\sigma/dP_{tW}d\eta_\gamma$ (pb/GeV) for the zero-jet process.

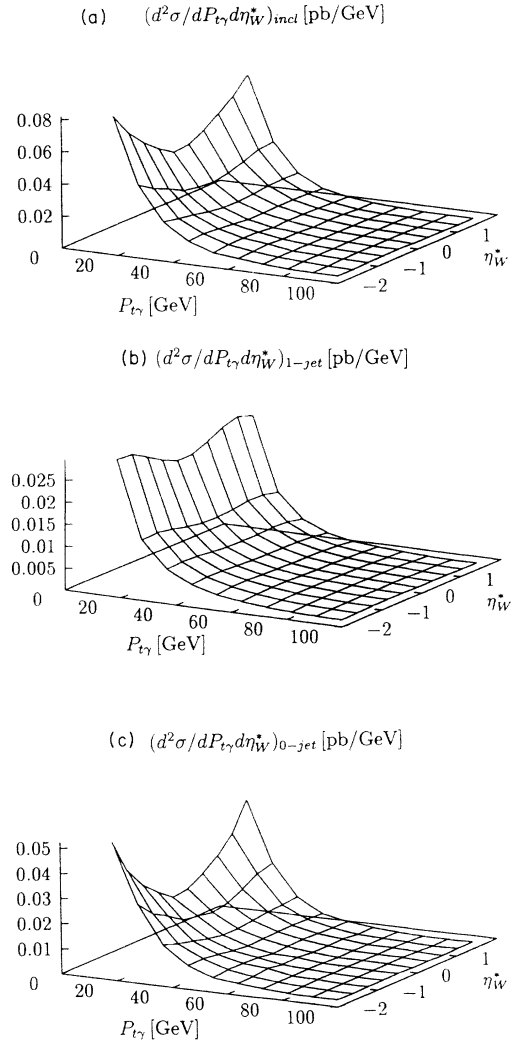

FIG. 34. (a) Two-body inclusive double differential cross section $d\sigma/dP_{t\gamma}d\eta^*_W$ (pb/GeV). (b) Double differential cross section $d\sigma/dP_{t\gamma}d\eta^*_W$ (pb/GeV) for the one-jet process. (c) Double differential cross section $d\sigma/dP_{t\gamma}d\eta^*_W$ (pb/GeV) for the zero-jet process.

regions of low $P_{t\gamma}$ [Figs. 29(a), 29(b), and 29(c)].

The $P_{t\,\mathrm{jet}}$ correlations with $P_{t\gamma}$ and P_{tW} are quite different: in the $P_{t\gamma}$ versus $P_{t\,\mathrm{jet}}$ space the events are mainly concentrated along the small $P_{t\gamma}$ and small $P_{t\,\mathrm{jet}}$ regions (see Fig. 35), while in the P_{tW} versus $P_{t\,\mathrm{jet}}$ space they are concentrated along the $P_{tW}=P_{t\,\mathrm{jet}}$ line (see Fig. 36). Something similar happens in the case of η_{jet} correlations with $P_{t\gamma}$ and P_{tW}: in the $P_{t\gamma}$ versus η_{jet} space the events are concentrated mainly along the small $P_{t\gamma}$ regions (see Fig. 42), while in the P_{tW} versus η_{jet} space they peak along the $P_{tW}=30$ GeV line (see Figs. 41 and 42).

Although the single rapidity distribution of the photon does not present a dip in the one-jet scenario (Fig. 11), the dip in η_γ reappears if we fix the rapidity of the jet, as can be appreciated in Fig. 37. The dip moves up in η_γ as

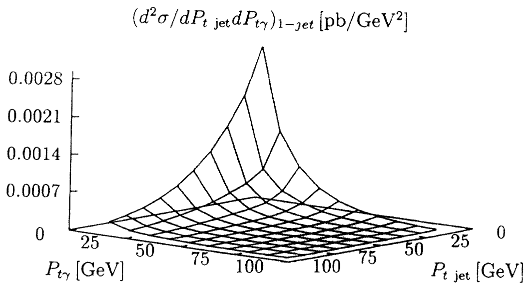

FIG. 35. Double differential cross section $d\sigma/dP_{t\,\mathrm{jet}}dP_{t\gamma}$ (pb/GeV^2) for the one-jet process.

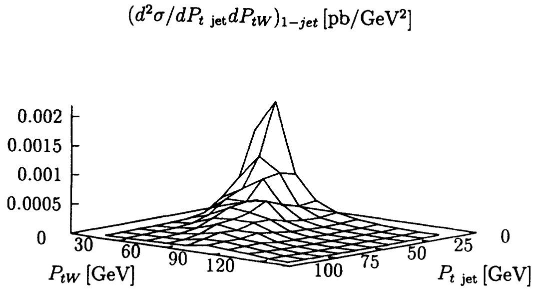

FIG. 36. Double differential cross section $d\sigma/dP_{t\,\text{jet}}dP_{tW}$ (pb/GeV^2) for the one-jet process.

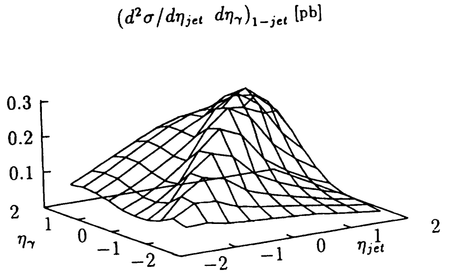

FIG. 37. Double differential cross section $d\sigma/d\eta_{\text{jet}}d\eta_\gamma$ (pb) for the one-jet process.

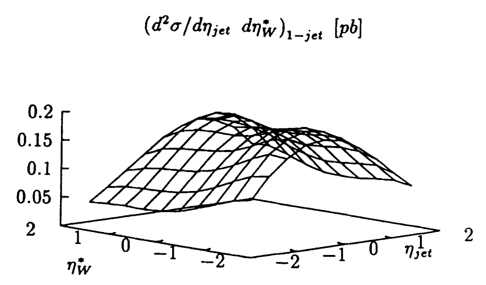

FIG. 38. Double differential cross section $d\sigma/d\eta_{\text{jet}}d\eta^*_W$ (pb) for the one-jet process.

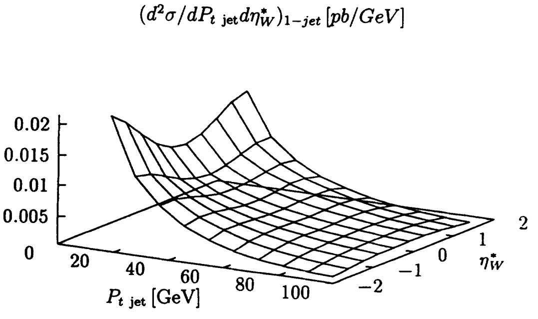

FIG. 39. Double differential cross section $d\sigma/dP_{t\,\text{jet}}d\eta^*_W$ (pb/GeV) for the one-jet process.

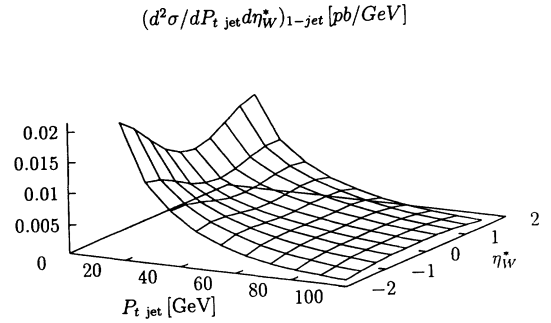

FIG. 40. Double differential cross section $d\sigma/dP_{t\,\text{jet}}d\eta_\gamma$ (pb/GeV) for the one-jet process.

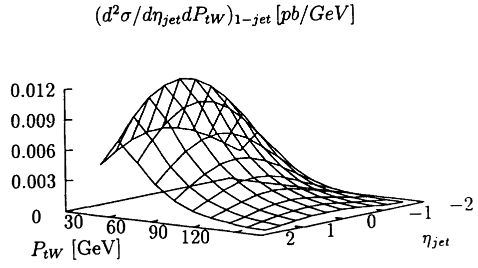

FIG. 41. Double differential cross section $d\sigma/d\eta_{\text{jet}}dP_{tW}$ (pb/GeV) for the one-jet process.

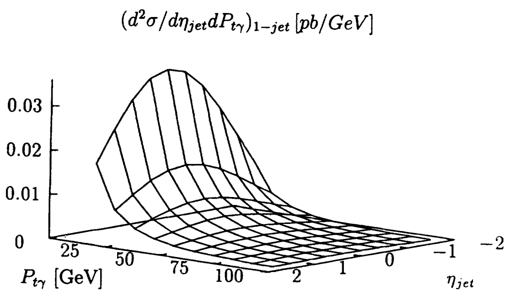

FIG. 42. Double differential cross section $d\sigma/d\eta_{\text{jet}}dP_{t\gamma}$ (pb/GeV) for the one-jet process.

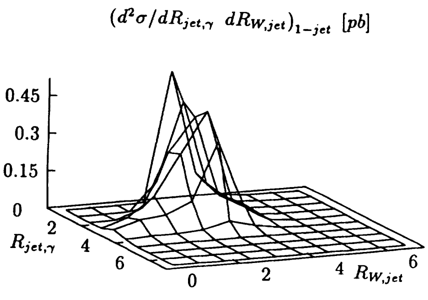

FIG. 43. Double differential cross section $d\sigma/dR_{\text{jet},\gamma}dR_{W,\text{jet}}$ (pb/GeV) for the one-jet process.

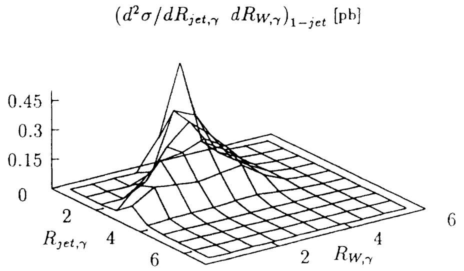

FIG. 44. Double differential cross section $d\sigma/dR_{\text{jet},\gamma}dR_{W,\gamma}$ (pb/GeV) for the one-jet process.

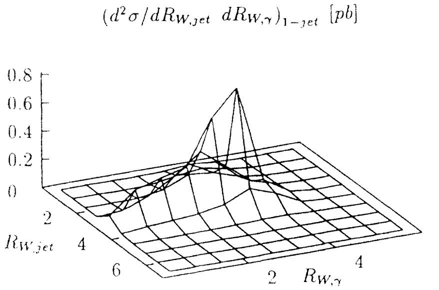

FIG. 45. Double differential cross section $d\sigma/dR_{W,\text{jet}}dR_{W,\gamma}$ (pb/GeV) for the one-jet process.

η_{jet} is increased and it is steeper in the regions of negative η_{jet}. This figure also shows that the double differential cross section peaks along the line as $\eta_\gamma = \eta_{\text{jet}}$.

Figures 43–45 show the correlations between cone sizes $R_{i,j}$. $R_{\text{jet},\gamma}$ versus $R_{W,\text{jet}}$ (Fig. 43) shows a symmetric shape around the plane $R_{W,\text{jet}} = \pi$ at which the correlation peaks with a dip around $R_{\text{jet},\gamma} = 1$; these features still show up in the single distributions in Fig. 21. The correlation of $R_{W,\text{jet}}$ with $R_{W,\gamma}$ (Fig. 45) peaks around $R_{W,\text{jet}} = R_{W,\gamma} = \pi$ and also has a symmetric shape with respect to the plane $R_{W,\text{jet}} = \pi$, confirming again the observations regarding the plot of $R_{W,\text{jet}}$ in Fig. 21. Although $R_{\text{jet},\gamma}$ versus $R_{W,\text{jet}}$ (Fig. 44) shows no simple symmetry, it also peaks near the planes $R_{\text{jet},\gamma} = \pi$ and $R_{W,\text{jet}} = \pi$. In general, the $R_{i,j}$ cone sizes peak around $R_{i,j} = \pi$ and fall off quickly above $R_{i,j} = 4$, and, in particular, $R_{W,\text{jet}}$ is symmetric around π even when plotted against other variables.

V. CONCLUDING REMARKS

We have completed an analysis of the exclusive reactions $p\bar{p} \to W^+\gamma$ and $p\bar{p} \to W^+\gamma + \text{jet}$ by generalizing the methodology used by other authors in the context of heavy quark and Z pair production,[8,9] which consistently includes all divergent regions of phase space in the framework of the factorization theorem and dimensional regularization. We have taken into account order α_S QCD corrections and leading logarithm bremsstrahlung contributions and used the latest CTEQ set of parton distribution functions, which fit the newly released HERA data. We have treated the W boson as a real particle with a mass of 80.2 GeV.

All our analytical results were presented in our paper [1] and have been used in a FORTRAN code with Monte Carlo integration techniques. Histograms of single and double differential cross sections and correlations for all outgoing particles (W boson, photon, and, when applicable, jet) have been obtained in each of three experimental scenarios, namely, two-body inclusive, one-jet, and zero-jet scenarios.

Our results for total, single, and double differential cross sections and correlations for the production of W^+ and photon accompanied by zero-jets show the smallest theoretical uncertainty under variations of the mass factorization and renormalization scales when compared with the predictions in the two-body inclusive and one-jet scenarios. This means that accurate predictions are available in the zero-jet scenario for quantities related to the W boson and the photon without including order α_S^2 corrections; however, they would have to be included for better accuracy in the other scenarios.

Previous work on the reaction $p\bar{p} \to W^+\gamma + X$ has been devoted to the study of single photon distributions, photon–W-boson pair mass, and photon–charged-lepton pseudorapidity correlations. The complete set of distributions and correlations including the W boson and the jet therefore complements the studies of the electroweak sector of the standard model (i.e., the magnetic moment of the W) and provides further checks for the QCD sector and the photon bremsstrahlung process. We note here that our results for the zero-jet and two-body inclusive reactions include leading logarithm photon fragmentation functions, so deviations of the observed experimental data from theoretical predictions could in part be accounted for by errors introduced by this approximation. To discriminate the effect of poorly known photon bremsstrahlung contributions from the effects of deviations from the standard model, the analysis of distributions and correlations in the one-jet scenario, which, at the present order in perturbation theory are free of photon bremsstrahlung, would provide a valuable tool. With regard to total cross sections the two reactions $p\bar{p} \to W^+\gamma$ and $p\bar{p} \to W^+\gamma + \text{jet}$ are of similar importance, but, as we pointed out before, the latter reaction really requires even higher order QCD corrections to provide more accurate predictions.

ACKNOWLEDGMENTS

S.M. would like to thank Professor D. Soper for some clarifying discussions during the CTEQ summer school. The work in this paper was supported in part by the contract NSF 9309888.

---

[1] S. Mendoza and J. Smith, preceding paper, Phys. Rev. D **50**, 226 (1994).

[2] G. P. Lepage, J. Comput. Phys. **27**, 192 (1978); "Vegas: an adaptive multi-dimensional integration program," Report No. CLNS-80/447, 1980 (unpublished).

[3] J. Botts, H. L. Lai, J. G. Morfín, J. F. Owens, J. Qiu, W. K. Tung, and H. Weerts, "Version 2 CTEQ distribution function in a parametrized form," obtained from H. L. Lai

(unpublished).

[4] D. W. Duke and J. F. Owens, Phys. Rev. D **26**, 1600 (1982).

[5] J. F. Owens, Rev. Mod. Phys. **26**, 465 (1987).

[6] J. Ohnemus and W. J. Stirling, Phys. Lett. B **298**, 230 (1993); J. Ohnemus, Phys. Rev. D **47**, 940 (1993); U. Baur, T. Han, and J. Ohnemus, *ibid.* **48**, 5140 (1993).

[7] S. Mendoza, J. Smith, and W. L. van Neerven, Phys. Rev. D **47**, 3913 (1993).

[8] M. L. Mangano, P. Nason, and G. Ridolfi, Nucl. Phys. **B373**, 295 (1992).

[9] B. Mele, P. Nason, and G. Ridolfi, Nucl. Phys. **B357**, 409 (1991); S. Frixione, M. L. Mangano, P. Nason, and G. Ridolfi, *ibid.* **B412**, 225 (1994).